Materials Today Communications 55 (2026) 115895

Contents lists available at ScienceDirect

Materials Today Communications

journal homepage: www.elsevier.com/locate/mtcomm

Pressure driven multi-phase transitions and atomic scale auxeticity in $CuCrSe_2$: A pathway to multifunctional metamaterials

Yun-Xia Jin [a], Xin-Zheng Li [b,c,d], Qi-Jun Ye [b,*]

[a] School of Electrical and Information Engineering, Yunnan Key Laboratory of Unmanned Autonomous System, Yunnan Minzu University, Kunming, Yunnan 650504, China
[b] State Key Laboratory for Artificial Microstructure and Mesoscopic Physics, Frontier Science Center for Nano-optoelectronics and School of Physics, Peking University, Beijing 100871, China
[c] Interdisciplinary Institute of Light-Element Quantum Materials, Research Center for Light-Element Advanced Materials, and Collaborative Innovation Center of Quantum Matter, Peking University, Beijing 100871, China
[d] Peking University Yangtze Delta Institute of Optoelectronics, Nantong, Jingsu 226010, China

ARTICLE INFO

Keywords:
DFT calculations
Multiferroic materials
Mechanical/Electronic properties
Multi-Phase Transitions

ABSTRACT

$(Cu,Ag)Cr(S,Se)_2$ materials are promising for spintronic and sensor applications, due to their known multi-ferroicity and superionic conductivity. Here, we report the concurrent pressure-induced phase transitions in $CuCrSe_2$ up to 50 GPa and its atomic-scale auxeticity by using first-principles calculations. With increasing pressure, the material undergoes phase transitions from normal solid to superionic state, semiconductor (SEMI) to metal, antiferromagnetic (AFM) to paramagnetic (PM), and normal compression to negative linear compressibility (NLC) and negative Poisson's ratio (NPR). To our knowledge, such a rich coexistence of phase transitions in a single material is rare, highlighting its potential for fine-tuning through diverse stimuli. By analyzing the atomic displacements and electronic structures, we reveal that the pressure-dependent lattice-electron-spin coupling plays a key role in regulating electron delocalization, disrupting magnetic order, and inducing these mechanical anomalies. Acoustic phonon softening simultaneously reduces the energy barrier for Cu ion diffusion, leading to a superionic state, and enables anomalous mechanical responses. These findings not only establish a novel platform for investigating multi-physics couplings but also provide insights for developing advanced functional materials.

Under hydrostatic pressure, most crystalline materials shrink in volume with a uniform reduction in all lattice parameters. In contrast, negative linear compressibility (NLC) refers to the expansion along a specific direction while maintaining overall volume compression, [1–3] as reported in inorganic oxides, [4] boride, [5] and sulfide [6] as well as metal-organic frameworks (MOF). [7–12] This counterintuitive response enables pressure-driven actuation and strain-amplification functions. A related mechanical anomaly is the negative Poisson's ratio (NPR), in which the material expands transversely when stretched longitudinally and thus are employed as impact-resistant structures and flexible electronics. [13–15] Accordingly, the coexistence of NLC and NPR within a single material would offer multifunctional capabilities under diverse stimuli like pressure and temperature. But such material is rarely reported and their underlying mechanisms are still poorly understood.

Most MOF materials exhibiting NLC and NPR rely on micro- or meso-scale geometric configurations, such as wine-rack like structures, [9,10] honeycomb structures, [11,16] and their hybrid networks, [17] to achieve anomalous mechanical responses. Their NLC behavior often arises along the longer diagonals of the organic framework, forming a spring-like topology under compression or decompression. However, these mechanisms typically require engineered architectures at relatively large scale, limiting miniaturization and integration into atomic scale devices. In contrast, inorganic materials can also show NLC when structural phase transitions occurs under high pressure. For example, NaB_3 exhibits a-axis expansion during a pressure induced phase transition from a tetragonal (*P4/mbm)* to an orthorhombic (*Pbam)* phase at ~16 GPa, which is primarily attributed to the symmetry breaking in the boron framework. [5] NLC along c-axis in γ-AlOOH nanotubes has been explained by the inflation associated with the incorporation of a

* Corresponding author.
E-mail address: qjye@pku.edu.cn (Q.-J. Ye).

https://doi.org/10.1016/j.mtcomm.2026.115895
Received 15 April 2026; Received in revised form 21 June 2026; Accepted 9 August 2026
Available online 10 August 2026
2352-4928/© 2026 The Authors. Published by Elsevier Ltd. This is an open access article under the CC BY-NC-ND license (http://creativecommons.org/licenses/by-nc-nd/4.0/).

pressure transmitting medium into the interior cavity of the tubular nanostructures. [4]

Meanwhile, inorganic material may also exhibit NPR due to structural motifs and electronic softening. Structurally, NPR often arises in materials with puckered or hinge-like structures, or in structures with low symmetry and non-centrosymmetric space groups (e.g., *P6$_2$m*, *P1*). For example, the puckered structures in black phosphorus, [18] Be_2C, [19] $GaPS_4$, [20] and $ScLaX_2$ (X = P, As, and Sb), [21] resembles a re-entrant structure with two coupled orthogonal hinges, enabling out-of-plane NPR under uniaxial deformation in the direction parallel to the pucker. Electronically, NPR materials feature weak chemical bonding and flexible bond strength, leading to low stiffness that allows large deformations and facilitates NPR. In SiC_6 siligraphene, the unique framework of sp^2 carbon and sp^3 silicon atoms can also lead to in-plane NPR, [22] while in β-Cu_2Se, the NPR arises from a strong electron-dominated intralayer interaction response. [23] Although high-throughput computational studies have predicted numerous NPR materials, the coexistence of NLC and NPR in a single inorganic material remains exceptionally uncommon.

$CuCrSe_2$, a non-van der Waals layered material, serves as an ideal platform for probing coupled NLC/NPR anomalies. Its multiferroicity, [24–26] narrow band gap (~0.16 eV), [27] superionic conductivity, [28] and exceptionally low lattice thermal conductivity [29,30] indicate a soft, highly responsive lattice where electronic, ionic, and mechanical responses can be tuned by pressure. Herein, its antiferromagnetic ordering is stabilized through Cr-Se-Cr superexchange, while vertical ferroelectric polarization arises from the tetrahedral coordination of Cu^+ ions. Both are bond-angle sensitive and thus directly coupled to lattice deformation. Moreover, the coexistence of $CrSe_6$ octahedra and $CuSe_4$ tetrahedra forms a scissor-like framework that allows hinge-like rotations, offering an atomic-scale route to NLC and NPR without relying on macroscopic architectures.

In this work, we explore the multi-phase transitions and anomalous mechanical properties of $CuCrSe_2$ under pressures from 0 to 50 GPa, by first principles density functional theory (DFT) calculations. Unlike the materials mentioned above, NLC and NPR in $CuCrSe_2$ lies in neither structural phase transition nor micro-architectures. These anomalous mechanical properties are achieved through atomic-scale hinge motions driven by bond length and angle adjustment. Normal solid state to superionic transitions is observed at 40 GPa. SEMI-to-metal and AFM-to-PM phase transitions are observed at 10 GPa and 35 GPa, respectively. Below 20 GPa, $CuCrSe_2$ exhibits conventional mechanical behavior, followed by NLC from 20 to 40 GPa and NPR from 40 to 50 GPa. By analyzing the crystal structure, magnetic order, and electronic properties, we elucidate the lattice-electron-spin coupling mechanisms driving these transitions. Under pressure, lattice compression enhances electron delocalization, disrupts magnetic order, and releases lattice degrees of freedom, thereby inducing NLC and NPR. These findings have deepened our understanding of multi-coupling physics under extreme conditions and highlight $CuCrSe_2$'s potential in designing auxeticity metamaterials, especially in high-precision piezotronic devices and shock-absorbing aerospace coating s operating under high pressures.

Density-functional theory (DFT) and *Ab initio* molecular dynamics (AIMD) simulations were performed using the Vienna Ab initio Simulation Package (VASP). [31,32] The ion-electron interaction was treated using the projected augmented wave (PAW) approach. [33] The exchange-correlation effects were described by Perdew-Burke-Ernzerhof (PBE) functional within the Generalized Gradient Approximation (GGA). [34] A plane-wave energy cutoff of 800 eV and a Gamma centered *k*-point mesh with a spacing of $2\pi \times 0.01$ Å^{-1} were used. During the ab initio calculations, the geometric structures were fully relaxed until that the force on each atom was less than 1×10^{-6} eV·Å^{-1}, and the maximum Hellman-Feynman force was smaller than 0.01 eV Å^{-1}. Spin polarization was incorporated in the simulations. For AIMD runs, a 2x2x2 supercell with a total of 96 atoms and an antiferromagnetic configuration along the c-axis was constructed from the conventional unit cell. Machine-learned force fields (MLFFs) were generated on the fly within the VASP framework during the AIMD simulations, which provided accurate interatomic forces to compute the force constants and phonon spectra via the finite displacement method using the Phonopy code. [35,36] Bonding strengths were obtained by the crystal orbital Hamilton population (COHP) method, which is implemented in the LOBSTER code. [37] In addition, the postprocessing of VASP data was performed by using VASPKIT and VESTA. [38,39]

Under ambient conditions, $CuCrSe_2$ adopts an Ilmenite-type structure crystallizing in the trigonal *R3m* space group. The chromium centers exist as Cr^{3+} ions, each coordinated by six Se^{2-} anions to form edge-sharing $CrSe_6$ octahedra. As shown in Fig. 3(a), these octahedral units exhibit a three-dimensional connectivity pattern, resulting in a characteristic bimodal distribution of Cr-Se bond length as three shorter ones of 2.52 Å and three longer ones of 2.63 Å. In the meantime, the copper ions (Cu^+) reside in distorted tetrahedral environments, forming a compressed tetrahedral geometry, with one shorter Cu-Se bond of 2.34 Å and three longer bonds of 2.49 Å. This dual coordination role of selenium atoms mediates the structural integration between chromium octahedra and copper tetrahedra, establishing a strongly correlated framework characteristic of Ilmenite-type chalcogenides.

The pressure evolutions of the crystalline structure and magnetic profile are presented Fig. 1. DFT calculations demonstrate the persistence of *R3m* space group symmetry across the entire pressure range, as evidenced by invariant Wyckoff positions (Cr: 3a; Cu: 3b; Se: 6c) and point-group operations. In the low-pressure regime (0–20 GPa), both in-plane (a-axis) and out-of-plane (c-axis) lattice parameters contract monotonically, as shown in Fig. 1(b). The compression along the *a*-axis is more sensitive to external pressure than that along the *c*-axis, with a larger relative reduction of −8.54% than −1.18% at 20 GPa. The overall unit-cell volume is normally compressed by a ratio of −17.3%, accompanied by cooperative intra- and interlayer lattice parameters shortening. In the intermediate regime (20–35 GPa), the *a*-axis and volume continue being contracted, while the *c*-axis exhibits anomalous expansion from −1.18–1.75% in relative change, indicating NLC. Concurrently, the Cr magnetic moments decrease gradually from 3.01 μB (0 GPa) to 2.20 μB (35 GPa).

We highlight the regime of 35–40 GPa, which manifests a synergy among triple phase transitions. As shown in Fig. 1(b)-(e), the collapse of magnetic order, inflection point of volume contraction rate, and abrupt expansion of c-axis demonstrate a concurrent pressure-driven AFM-to-PM, NLC-to-PLC, and PPR-to-NPR phase transition. The synchronicity of these three phenomena implies strong coupling among lattice, magnetic order, and electronic states.

To evaluate the structural stability and dynamic behavior under high pressure, we performed AIMD and phonon spectra calculations for $CuCrSe_2$ at 0, 20, and 40 GPa. As shown in Fig. 2(a), the atomic arrangement remains ordered in the *b-o-c* plane at all pressures. In the *a-o-b* plane, the structure remains well-ordered at 0 GPa, while at 40 GPa it becomes highly disordered, exhibiting a characteristic of superionic behavior. Fig. 2(b) displays the evolution of the total energy during the AIMD simulations. At all three pressures, the energy curves level off and fluctuate around a constant value, indicating that the systems have reached equilibrium. The total energy increases with increasing pressure. Representative snapshots extracted from the AIMD trajectories at 1, 2, 5, and 10 ps confirm that the structures remain stable throughout the simulation period at 40 GPa. The mean squared displacement (MSD) was monitored over a 10 ps simulation time. At 0 and 20 GPa, the MSD values remain very low and essentially flat, indicating negligible long-range diffusion. In contrast, at 40 GPa the MSD increases linearly with time, revealing substantial long-range diffusion of Cu ions. The diffusion coefficient of Cu ions is calculated to be 1.93×10^{-5} cm^2/s. This is slightly higher than this experimental value (7.2×10^{-6} cm^2/s at 495 K and ambient pressure), as a competing result between the higher pressure (enhancing it) and lower temperature (reducing it). [28] This behavior signals a pressure induced transition to a superionic-like phase, where

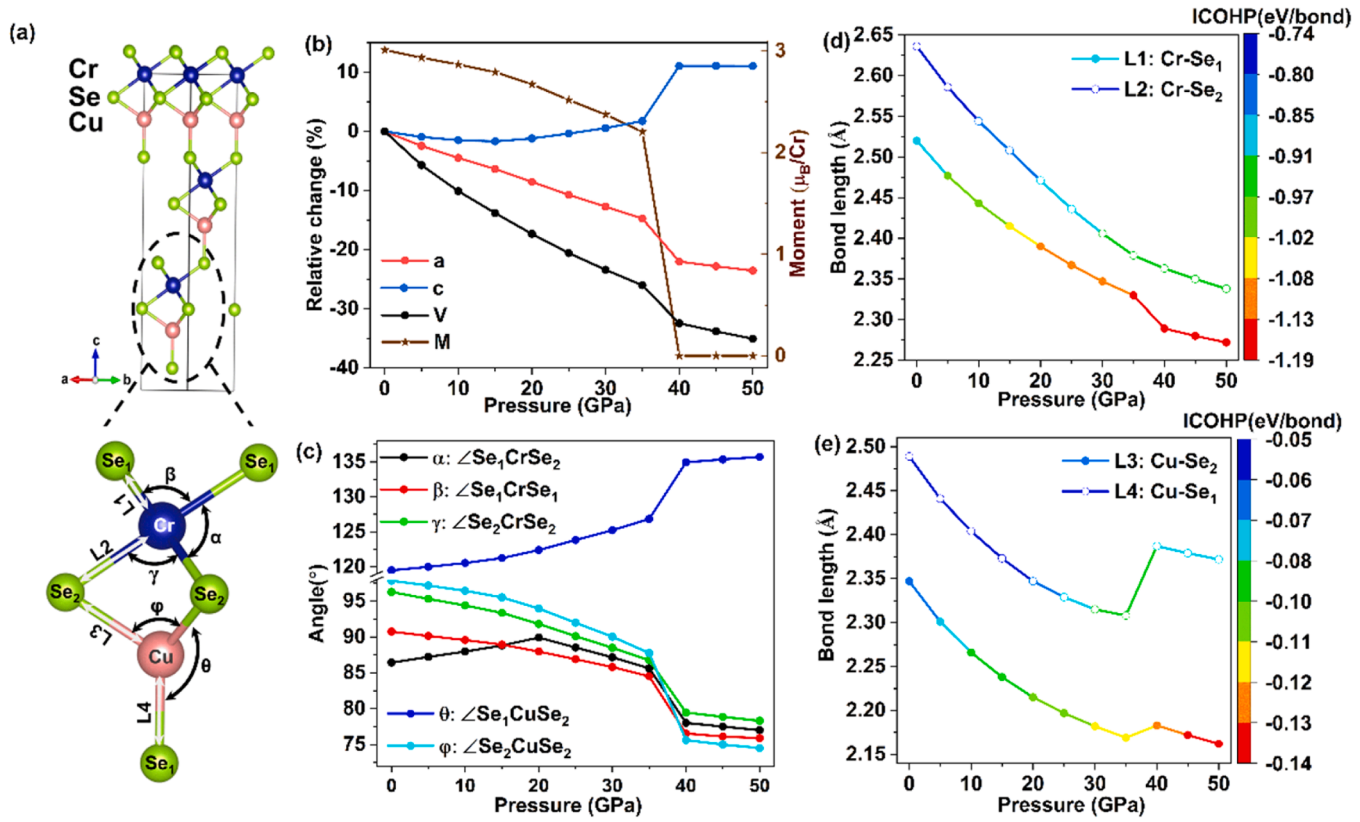

Fig. 1. (a) Schematic representation of the crystal structure of $CuCrSe_2$. Green, blue, and pink spheres denote Se, Cr, and Cu atoms, respectively. (b) Relative change in the lattice parameters and volume, local magnetic moment of Cr atoms as a function of pressure. (c) Pressure-dependent evolution of interlayer and intralayer bond angles for Se-Cr-Se (α, β, γ) and Se-Cu-Se (θ, φ) coordination geometries. (d)-(e) Bond length variations of Cr-Se (L_1, L_2) and Cu-Se (L_3, L_4) with pressure, color-mapped to ICOHP values, where cooler (warmer) hues indicate weaker (stronger) covalent interactions.

Cu ions become mobile within the lattice. To reveal the evolution of the local atomic structure under high pressure, we calculated the pair distribution functions (PDFs) for Cu-Se, Cr-Se, and Se-Se atomic pairs at different pressures (0, 20, and 40 GPa), as shown in Fig. 2(d)-(f). At ambient pressure, the characteristic peaks for Cu-Se, Cr-Se, and Se-Se pairs are located at approximately 2.42 Å, 2.58 Å, and 3.73 Å, respectively. As pressure increases to 20 GPa, all characteristic peaks shift significantly towards lower r values, indicating a general compression of interatomic distances and enhanced short-range bonding under pressure. The main peak of the Cr-Se and Se-Se pair shifts to lower r and remains sharp at 40 GPa, indicating that the Cr-Se framework retains its stability under high pressure. In contrast, the Cu-Se peaks show decreased intensity, broadened width, and disappearance of secondary peaks at higher r, reflecting superionic characteristics.

Phonon dispersions and the corresponding phonon density of states (DOS) were also computed. At 0 and 20 GPa, all phonon branches lie in the positive frequency region, confirming dynamical stability. At 40 GPa, however, pronounced imaginary frequencies appear near high-symmetry points and along connecting paths in the Brillouin zone. Concurrently, the phonon DOS exhibits an anomalous peak below 0 THz. These imaginary modes indicate strong anharmonic softening under pressure, while they appear as instabilities within the treatment of harmonic approximation.

Under high pressure, particularly near or within the superionic phase, the atomic motion in $CuCrSe_2$ exhibits strong anharmonicity. The imaginary frequencies appearing in the phonon spectrum reflect soft mode instabilities within the harmonic approximation. Such instabilities can be released through two pathways: global structural collapse or partial disordering of a specific sublattice while the host framework remains intact. In fact, $CuCrSe_2$ belongs to the latter case: AIMD simulations show that at 40 GPa, the Cr-Se framework does not undergo global collapse, while the Cu sublattice becomes dynamically disordered and enters a superionic state with highly mobile Cu ions. Consistent with this, AIMD simulations show no structural collapse but reveal rapid Cu-ion diffusion, reflected by the linear rise in MSD. We therefore interpret the 40 GPa state as a transition from an ordered solid phase to a superionic or liquid-like phase with high ionic conductivity. Similar pressure or temperature induced transitions to superionic phases have been widely reported in related chalcogenide materials, such as $AgCrSe_2$ and Ag_8SnSe_6, as well as in lithium-based fast-ion conductors. [29,40] Therefore, for subsequent calculations of mechanical properties, we employed the perfect structure at 40 GPa.

High pressure induces softening of the acoustic branches, which significantly reduces the energy barriers for ion diffusion, promoting the emergence of a superionic state. It also implies a reduction in the rigidity of interatomic forces, making the lattice more susceptible to be deformed, thereby facilitating anomalous responses such as NPR. In the discussion of mechanical properties in subsequent, we observed that NPR emerges at 40 GPa. These two phenomena might be different manifestations of the same lattice instability.

The pressure-dependent mechanical properties of $CuCrSe_2$, including the elastic tensor and the moduli, provide insights into its stability and anomalous response under hydrostatic compression. For the trigonal crystal symmetry of $CuCrSe_2$, there are six independent elastic constants (C_{11}, C_{12}, C_{13}, C_{33}, C_{14}, C_{44}). As shown in Fig. 3(a), most elastic constants harden monotonically with increasing pressure, while C_{44} has a negative slope. Throughout the 0–50 GPa, the elastic constants satisfy the Born-Huang stability criteria (C_{11} - C_{12} >0; $C_{13}^2 < 0.5*C_{33}*(C_{11}+C_{12})$; $C_{14}^2 < 0.5*C_{44}*(C_{11}-C_{12})$; $C_{44} > 0$). [41] Notably, C_{33} grows more rapidly than C_{11}, indicating a significant anisotropic compression behavior: the [001] direction possesses **larger resistance to compression** than the [100] direction. Above 40 GPa, both C_{11} and C_{33} exhibit accelerated increases,

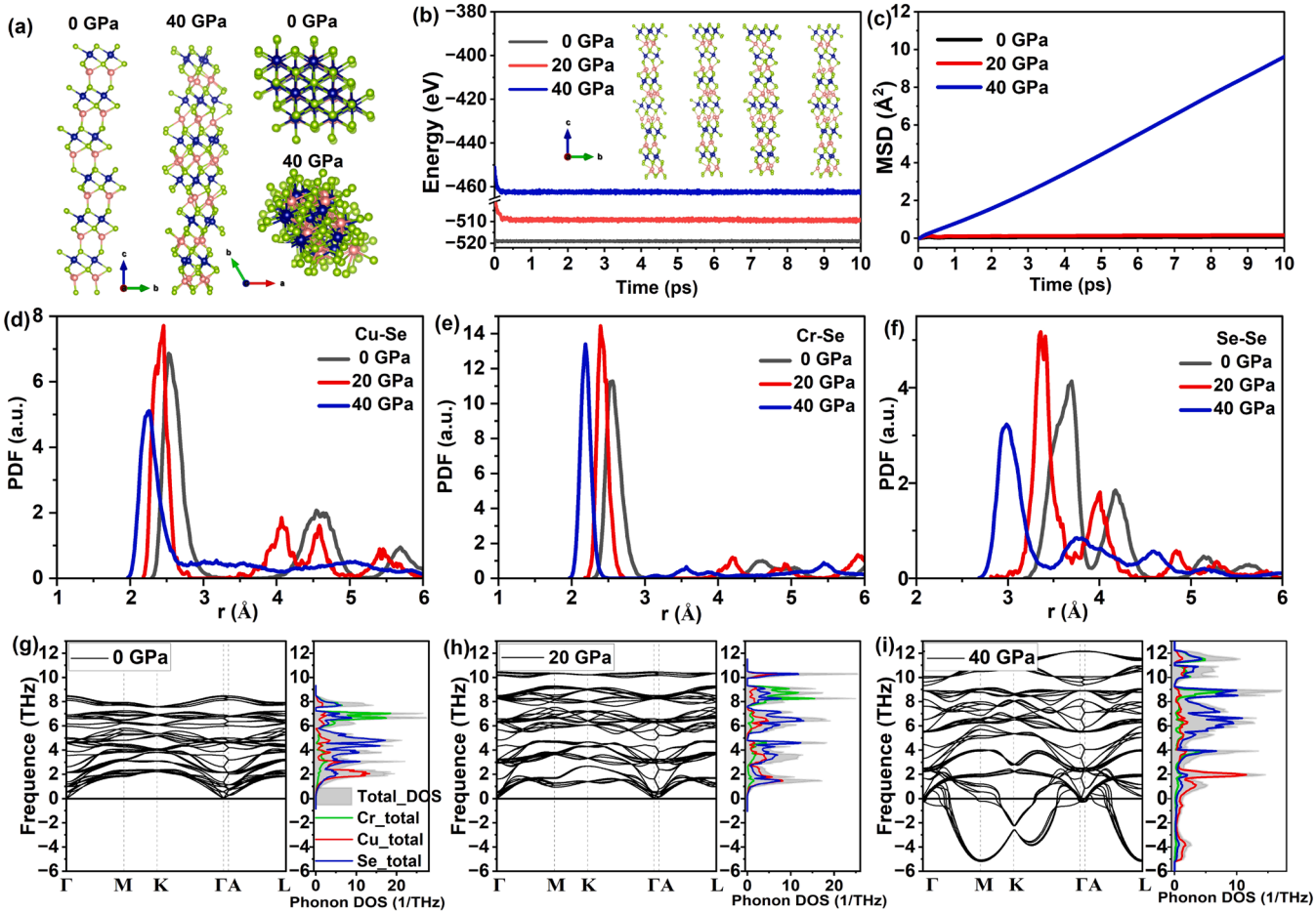

Fig. 2. (a) Crystal structures of solid and superionic state $CuCrSe_2$ obtained after 10 ps of AIMD simulation at 300 K under 0 GPa and 40 GPa. (b) Total energy at 300 K under different pressures. Inset images are representative snapshots from AIMD trajectories at 1, 2, 5, and 10 ps. (c) MSD of Cu atoms at 300 K under different pressures. (d)-(f) PDFs for Cu-Se, Cr-Se, and Se-Se atomic pairs at different pressures. (g)-(i) The phonon dispersion and phonon DOS at 300 K under different pressures.

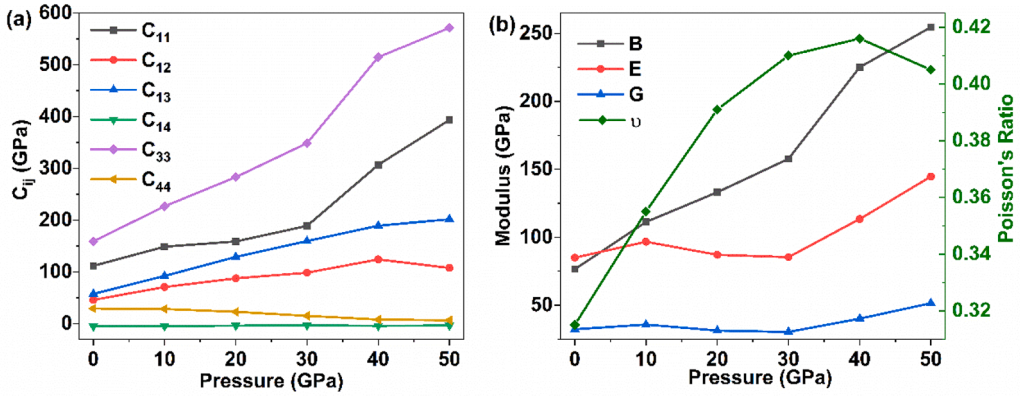

Fig. 3. Elastic tensor (C_{ij}) (a) and mechanical properties based on the VRH averages (b) variation of $CuCrSe_2$ under pressure.

coinciding with the AFM-to-PM phase transition. Furthermore, the negative value of C_{14} signify NLC, the counterintuitive response in which shear deformation induces lattice expansion.

Fig. 3(b) presents the Voigt-Reuss-Hill (VRH) averages of the bulk modulus (B), Young's modulus (E), shear modulus (G), and Poisson's ratio (ν) under pressure. [42] Both B and E increase with pressure, implying that $CuCrSe_2$ becomes harder and more incompressible. Remarkably, NLC emerges within the 20–40 GPa pressure interval, and NPR is observed between 40 and 50 GPa. Beyond 40 GPa where the AFM-PM phase transition occurs, they exhibit an accelerated growth rate, mirroring the trend of C_{11} and C_{33}. In the meantime, shear modulus G shows slight increase with pressure, implying limited resistance to shape distortion despite enhanced volumetric stiffness. The Poisson's ratio ν displays non-monotonic pressure dependence: it initially increases from 0.315 to 0.416 between 0 and 40 GPa, due to stress redistribution under compression, and then decreases to 0.405 at

50 GPa, seemingly linked to the NPR in certain directions.

To explore such directional dependencies, we visualize the angular variation of linear compressibility (β) and Poisson's ratio (ν). As shown in Fig. 4(a)-(c), β is isotropic along [001] but exhibits larger magnitudes than along [100], implying greater sensitivity to pressure along the out-of-plane direction. This is contrary to expectations for layered materials with weak interlayer bonds yet aligned with the observed *c*-axis expansion in Fig. 1. Anisotropy along [100] are enhanced with pressure, and since 20 GPa, negative β emerges along the *c*-axis (90° orientation), where the NLC emerges. The Poisson's ratio also varies directionally. Due to the graphene-like honeycomb atomic network of $CrSe_6$ octahedra and $CuSe_4$ tetrahedra imposed by trigonal crystal, 60° periodic distributions are observed in the polar plot for both min and max values of ν along [001], as shown in Fig. 4(d)-(f). Here, the in-plane high-symmetry crystallographic orientations restrict and enhance transverse deformation under longitudinal strain, respectively. The data of these mechanical properties are detailed in Table 1, with further ones including anisotropic ratios (A_E, A_G). The anisotropy ratios A_E and A_G gradually increase with pressure, in alignment with the symmetry-preserving structural evolution observed in Fig. 1.

To elucidate the atomic-scale origins, we analyze the pressure dependent bond geometries. As depicted in Fig. 1(a), the $CuCrSe_2$ structure consists of alternating V-shaped Se-Cr-Se and Se-Cu-Se units via shared Se atoms along the [001] direction, with each resembling scissor-like framework. In mediating pressure responses, their bond angle adjustments might be more influential than bond length variation, since they enable structural reconfiguration without significant energy costs in bond stretching.

In the low-pressure range (0–35 GPa), the intralayer Se-Cr-Se and Se-Cu-Se angles, as β, γ-angle and φ-angle, progressively decrease, and interlayer Se-Cu-Se angles, as θ-angle in Fig. 1(a), monotonically increase, indicating enhanced buckling and hence in-plane contraction. The shortening of Cr-Se and Cu-Se bonds, coupled with increasingly negative ICOHP values, implies enhanced orbital overlap under compression. Accordingly, this strengthening of metal-ligand bonding drives the conventional contraction of the *a*-axis and *c*-axis, as expected as typical positive compressibility. Notably, the θ-angle decreases in 20–35 GPa, restoring a local Cr-centered octahedral geometry, in contrast to its behavior in 0–20 GPa. Despite continued bond shortening, the counteracting effects of scissor and intralayer buckling yield net *c*-axis expansion (NLC onset), while *a*-axis persists compression.

In the critical regime (35–40 GPa), all these bond angles experience abrupt changes against their original trend, accompanied by anomalous elongation of next-nearest Cu-Se bonds (*L3* and *L4* in Fig. 1(a)) despite stronger ICOHP interaction. This is associated with an AFM-to-PM phase transformation. Below 35 GPa, the gradual unwinding of the scissor (increase in α-angle) dominates over bond contraction, driving *c*-axis expansion. Above 35 GPa, ligand field reorganization enhances Cu-Se covalency while elongating Cu-Se bonds, likely through *d-p* orbital rehybridization. This dual effect induces a sudden dilation of the *c*-axis. Above 40 GPa and under the PM phase, the NPR manifests as *a*-axis contraction due to intralayer buckling and accommodated *c*-axis expansion. This process is mediated by flexible metal-ligand bonds and electron reconstruction therein. At 40 GPa, the rapid diffusion of Cu ions in superionic $CuCrSe_2$ renders the lattice more flexible, where these diffusing ions serve as lubricant. When the lattice attempts to undergo deformation under pressure toward NPR, these mobile ions promote the rapid reconstruction and relaxation of the atomic arrangement, thereby stabilizing and enhancing the NPR effect.

Following the bond geometry analysis in previous section, which revealed how bond angle reconfiguration within the scissor-like framework drives NLC and NPR, we now focus on the underlying electronic mechanisms governing structural and mechanical anomalies. The pressure induced electronic reconstructions are probed by the spin-polarized electronic band structure, partial density of states (PDOS), and electron localization function (ELF). At ambient pressure, the high ELF around Se atoms, signifies localized lone-pair electrons, whereas the low electron density in the interlayer Se-Cu-Se region indicates ionic bonding and weak interlayer coupling. With pressure increases, Cr-Se bonds become more covalent and the bandgap is narrowed due to band broadening. Thus, $CuCrSe_2$ experiences a SEMI-to-metal phase transition, evidenced by the Fermi level intersecting the conduction

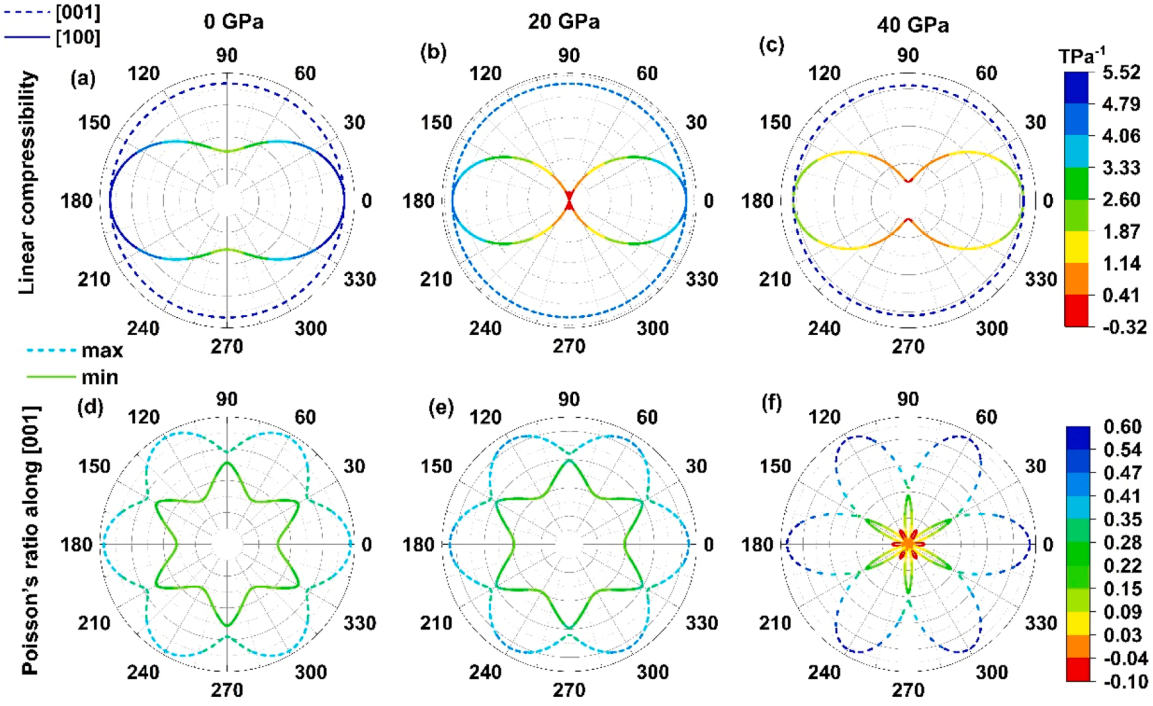

Fig. 4. Linear compressibility and Poisson's ratio of $CuCrSe_2$ under 0, 20 and 40 GPa. The dashed outer line and solid inner line are linear compressibility along [001] and [100] direction in (a)-(c). The dashed outer line and solid inner line are the maximum and minimum values in (d)-(f).

Table 1
The Young's modulus E (GPa), shear modulus G (GPa), linear compressibility β (TPa^{-1}), Poisson's ratio υ and anisotropic ratio (A_E, A_G) of $CuCrSe_2$ bulk single crystal under various pressure.

Pressure (GPa)	Elastic property										
	Young's modulus (GPa)			Shear modulus (GPa)			Linear compressibility (TPa^{-1})			Poisson's ratio	
	E_{min}	E_{max}	A_E	G_{min}	G_{max}	A_G	β_{min}	β_{max}		ν_{min}	ν_{max}
0	68.62	117.08	1.71	25.61	38.34	1.49	2.31	5.51	0.159		0.506
10	74.69	149.15	1.99	26.42	45.48	1.72	1.07	4.11	0.171		0.614
20	64.00	148.26	2.32	21.63	40.77	1.89	−0.31	4.23	0.169		0.710
30	49.05	171.34	3.49	14.72	46.85	3.18	−0.65	3.84	0.076		0.845
40	28.03	348.92	12.45	7.59	101.78	13.42	0.35	2.17	−0.079		0.976
50	24.93	409.04	16.41	6.53	142.95	21.88	0.48	1.80	−0.103		0.978

Table 2
Pressure-Dependent Electronic, Magnetic, and Elastic Properties. Pressure ranges are defined inclusively for the lower bound and exclusively for the upper bound (e.g., [0, 10) includes 0 GPa but excludes 10 GPa).

Pressure range (GPa)	Electron structure	Magnetic property	Linear compressibility	Poisson's ratio
[0, 10)	SEMI	AFM	PLC	PPR
[10, 20)	metal	AFM	PLC	PPR
[20, 40)	metal	AFM	NLC	PPR
[40,50]	metal	PM	PLC	NPR

bands above 10 GPa, with prominent metallic character established at 40 GPa. Especially, the Cr *d*-electrons shift towards the Fermi level, forming electron delocalization channels that lead to metallization. Concurrently, ELF shows a more uniform electron distribution within Se-Cr-Se intralayer, reflecting strengthened *d-p* hybridization.

In contrast, compression along *c*-axis is affected by electron delocalization above 20 GPa. In the interlayer region, a continuous distribution of Se *s*- and Cu *d*-electrons through the Cu-Se channels is formed, enhancing the charge bridging effect. This is evidenced by their broader PDOS peaks and color evolution of ELF profiles in Fig. 5(f)-(i). The magnetic order collapse releases spin-induced pinning constraints that stabilize the crystal structure, freeing rotational degrees of freedom in the scissor-like framework, enabling interlayer sliding via increased Cu-Se bond angles, and facilitating NLC. At pressures above 40 GPa, the reduced separation between the Cu layer and the Cr-Se framework is accompanied by pronounced electronic rearrangement in the interlayer region, as indicated by the ELF profiles in Fig. 5(i). This suggests enhanced interlayer interaction, which may be associated with the emergence of NPR.

Under pressure, the synergistic effects of geometric mismatch and electron delocalization disrupt the superexchange interaction in $CuCrSe_2$. Firstly, the shortened Cr-Se bond lengths and distorted bond angles break the geometry required for superexchange mechanism of Cr. As a result, the Se atoms no longer act as mediators for spin transfer between antiferromagnetically coupled Cr ions, instead forming a charge screening layer that disrupts local magnetic moments and blocks the transmission of spin information. Secondly, the band energy of the Se *4p*-orbital shifts downward (becoming more negative), widening the energy gap with the Cr *3d* orbitals. This enlarged gap between Se and Cr reduces hybridization efficiency and inhibits spin transmission. This shift replaces spin-mediated superexchange with charge flow, contributing to metallization and collapse of the superexchange pathway. Thirdly, the Cr *3d* band broadens due to electrons transfer from Cr to Se, also diminishing the local magnetic moment of Cr. These factors collectively induce the AFM-to-PM phase transition.

In recent years, high-throughput computational studies have predicted a large number of NPR materials, however, the NLC and NPR coexisting in on single inorganic material is extremely rare. The mechanism of NLC and NPR in $CuCrSe_2$ is the cooperative deformation capability of its coordination polyhedral, where pressure-induced lattice-electron-spin coupling drives electron delocalization and magnetic order collapse. This leads to concurrent multi-phase transitions and tunable anomalies by pressure. Similar properties and mechanisms can be extended to analogous structures containing flexible metal sites (e.g., tetrahedral coordination of Cu/Ag/Au/Pd/Pt), rigid transition metal frameworks (e.g., octahedral networks of Cr/Mo/Co/Nb), and non-centrosymmetric layered frameworks. Using descriptors such as bond angle adjustability, covalent bond strength, and magnetic-lattice correlation, combined with machine learning-assisted design, holds promise for discovering the universality of anomalous mechanical properties in similar structural materials. This approach will advance the development of mechanical metamaterials.

Under pressure from 0 to 50 GPa, we observe that $CuCrSe_2$ undergoes multi-phase transitions from SEMI to metal, AFM to PM, and normal compression to NLC and NPR, establishing it as a promising candidate for multi-functional metamaterials. Unlike the bond length shortening mechanism in conventional materials under high pressure, the bond angle variation determines the abnormal mechanical response in $CuCrSe_2$. With pressure increases, the covalency of Cr-Se firstly enhances, manifesting a transition of electrons from delocalization to metallization. This metallization weakens superexchange interactions, transforming selenium from a spin mediator to a charge screening layer, thereby triggering magnetic order collapse. This collapse releases the spin-induced pinning constraints, thereby unwinding the structural stabilization and inducing both NLC and NPR. These findings provide a novel platform for exploring multi-physics couplings and suggest that descriptors such as bond angle adjustability and magnetic-lattice correlation, combined with machine learning, can guide the discovery of similar materials.

CRediT authorship contribution statement

Yun-Xia Jin: Writing – original draft, Methodology, Investigation, Formal analysis, Data curation, Conceptualization. **Xin-Zheng Li:** Supervision, Project administration, Funding acquisition. **Qi-Jun Ye:** Writing – review & editing, Supervision, Project administration, Formal analysis.

Funding

This work is supported by the National Science Foundation of China under Grants No. 12204015, No. 12234001, No. 12474215, and No.

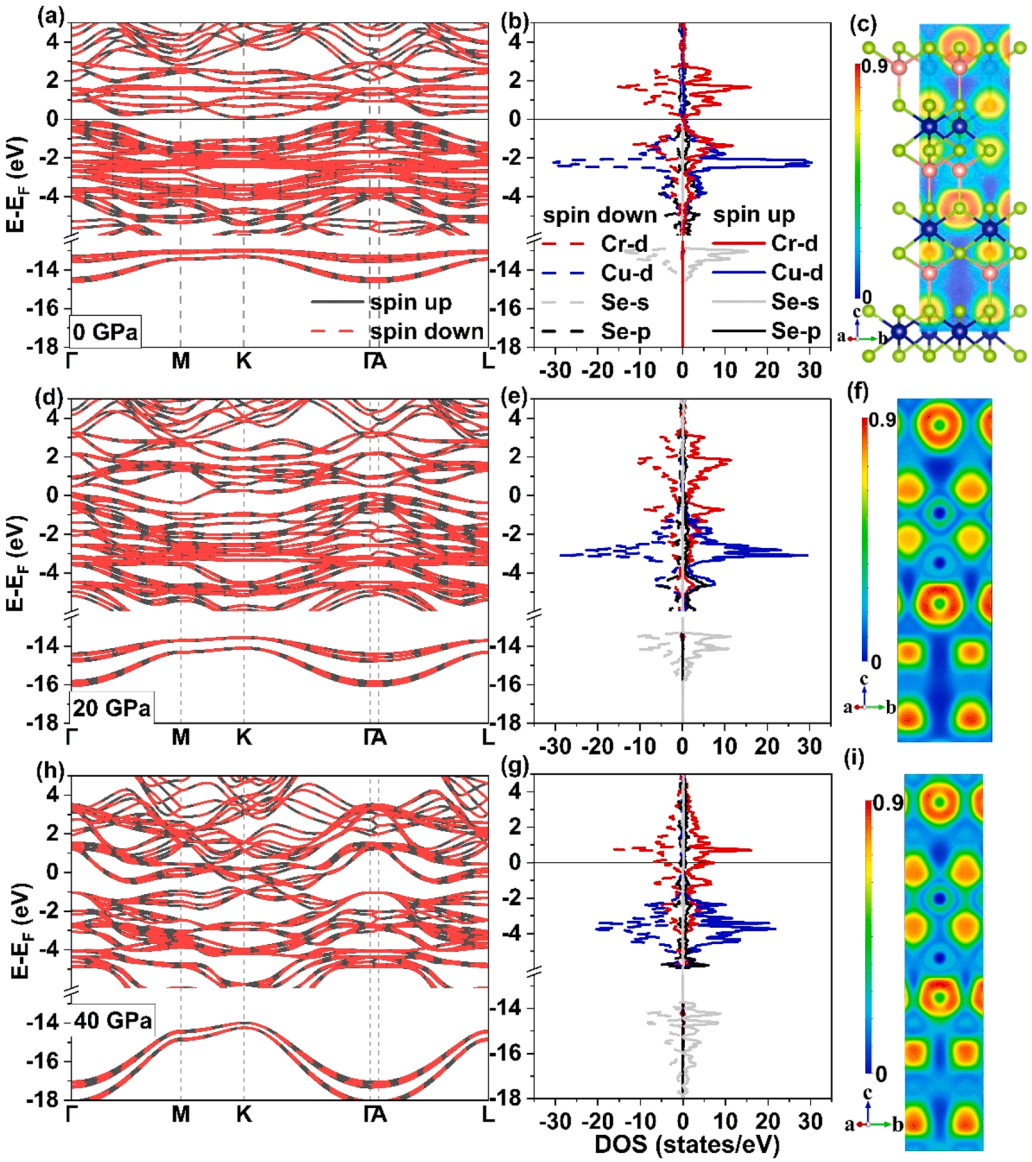

Fig. 5. Band structure (a, d, h), partial density of states (PDOS) (b, e, g), and electron localization function (ELF) (c, f, i) for $CuCrSe_2$ at 0, 20, and 40 GPa.

62321004, the National Basic Research Program of China under Grants No. 2021YFA1400500 and No. 2022YFA1403500.

Declaration of Competing Interest

The authors declare that they have no known competing financial interests or personal relationships that could have appeared to influence the work reported in this paper.

Data Availability

Data will be made available on request. The data that support the findings of this study are available from the corresponding authors on reasonable request.

References

[1] R.H. Baughman, S. Stafström, C. Cui, S.O. Dantas, Materials with Negative Compressibilities in One or More Dimensions, Science 279 (1998) 1522–1524, https://doi.org/10.1126/science.279.5356.1522.

[2] A.D. Fortes, E. Suard, K.S. Knight, Negative Linear Compressibility and Massive Anisotropic Thermal Expansion in Methanol Monohydrate, Science 331 (2011) 742–746, https://doi.org/10.1126/science.1198640.

[3] A.B. Cairns, A.L. Goodwin, Negative linear compressibility, Phys. Chem. Chem. Phys. 17 (2015) 20449–20465, https://doi.org/10.1039/C5CP00442J.

[4] X. Xing, Z. Wei, L. Jiang, J. Zhang, Y. Luo, Y. Ma, Q. Cui, Abnormal compression behavior with unexpected negative linear compressibility of γ -AlOOH nanotubes, Appl. Phys. Lett. 125 (2024) 093102, https://doi.org/10.1063/5.0220523.

[5] X.-L. He, S.-N. Pan, Y. Chen, X.-J. Weng, Z. Wang, D. Yu, X. Dong, J. Sun, Y. Tian, X.-F. Zhou, Negative linear compressibility and unusual dynamic behavior of NaB 3, Phys. Rev. Mater. 5 (2021) 035002, https://doi.org/10.1103/PhysRevMaterials.5.035002.

[6] A. Marmier, P.S. Ntoahae, P.E. Ngoepe, D.G. Pettifor, S.C. Parker, Negative compressibility in platinum sulfide using density-functional theory, Phys. Rev. B 81 (2010) 172102, https://doi.org/10.1103/PhysRevB.81.172102.

[7] W. Li, M.R. Probert, M. Kosa, T.D. Bennett, A. Thirumurugan, R.P. Burwood, M. Parinello, J.A.K. Howard, A.K. Cheetham, Negative Linear Compressibility of a Metal–Organic Framework, J. Am. Chem. Soc. 134 (2012) 11940–11943, https://doi.org/10.1021/ja305196u.

[8] Q. Zeng, K. Wang, B. Zou, Abnormal Compressive Behaviors of Metal–Organic Frameworks under Hydrostatic Pressure, Langmuir 38 (2022) 9031–9036, https://doi.org/10.1021/acs.langmuir.2c01055.

[9] Q. Zeng, K. Wang, B. Zou, Negative Linear Compressibility Response to Pressure in Multitype Wine-Rack Metal–Organic Frameworks, ACS Mater. Lett. 2 (2020) 291–295, https://doi.org/10.1021/acsmaterialslett.9b00401.

[10] A.B. Cairns, A.L. Thompson, M.G. Tucker, J. Haines, A.L. Goodwin, Rational Design of Materials with Extreme Negative Compressibility: Selective Soft-Mode Frustration in $KMn[Ag(CN)_2]_3$, J. Am. Chem. Soc. 134 (2012) 4454–4456, https://doi.org/10.1021/ja204908m.

[11] A.L. Goodwin, D.A. Keen, M.G. Tucker, Large negative linear compressibility of $Ag_3[Co(CN)_6$, Proc. Natl. Acad. Sci. 105 (2008) 18708–18713, https://doi.org/10.1073/pnas.0804789105.
[12] S.G. Duyker, V.K. Peterson, G.J. Kearley, A.J. Studer, C.J. Kepert, Extreme compressibility in LnFe(CN)6 coordination framework materials via molecular gears and torsion springs, Nat. Chem. 8 (2016) 270–275, https://doi.org/10.1038/nchem.2431.
[13] R.H. Baughman, J.M. Shacklette, A.A. Zakhidov, S. Stafström, Negative Poisson's ratios as a common feature of cubic metals, Nature 392 (1998) 362–365, https://doi.org/10.1038/32842.
[14] K.K. Dudek, L. Mizzi, J.A. Iglesias Martínez, A. Spaggiari, G. Ulliac, R. Gatt, J. N. Grima, V. Laude, M. Kadic, Micro-scale graded mechanical metamaterials exhibiting versatile Poisson's ratio, Compos. Struct. 319 (2023) 117151, https://doi.org/10.1016/j.compstruct.2023.117151.
[15] K.K. Saxena, R. Das, E.P. Calius, Three Decades of Auxetics Research − Materials with Negative Poisson's Ratio: A Review, Adv. Eng. Mater. 18 (2016) 1847–1870, https://doi.org/10.1002/adem.201600053.
[16] G. Qin, Z. Qin, Negative Poisson's ratio in two-dimensional honeycomb structures, Npj Comput. Mater. 6 (2020) 51, https://doi.org/10.1038/s41524-020-0313-x.
[17] L. Wang, H. Luo, S. Deng, Y. Sun, C. Wang, Uniaxial Negative Thermal Expansion, Negative Linear Compressibility, and Negative Poisson's Ratio Induced by Specific Topology in $Zn[Au(CN)_2]_2$, Inorg. Chem. 56 (2017) 15101–15109, https://doi.org/10.1021/acs.inorgchem.7b02416.
[18] J.-W. Jiang, H.S. Park, Negative poisson's ratio in single-layer black phosphorus, Nat. Commun. 5 (2014) 4727, https://doi.org/10.1038/ncomms5727.
[19] S. Qian, X. Sheng, Y. Zhou, X. Yan, Y. Chen, Y. Huang, X. Huang, E. Feng, W. Huang, Two-Dimensional Be_2C with Octacoordinate Carbons and Negative Poisson's Ratio, J. Phys. Chem. C. 122 (2018) 7959–7967, https://doi.org/10.1021/acs.jpcc.7b12758.
[20] J.-H. Yuan, K.-H. Xue, J.-F. Wang, X.-S. Miao, Gallium Thiophosphate: An Emerging Bidirectional Auxetic Two-Dimensional Crystal with Wide Direct Band Gap, J. Phys. Chem. Lett. 10 (2019) 4455–4462, https://doi.org/10.1021/acs.jpclett.9b01611.
[21] X. Tian, X. Xie, J. Li, X. Kong, W.-J. Gong, F.M. Peeters, L. Li, Multiferroic ScLa X 2 (X = P, As, and Sb) monolayers: Bidirectional negative Poisson's ratio effects and phase transformations driven by rare-earth (main-group) elements, Phys. Rev. Mater. 8 (2024) 084407, https://doi.org/10.1103/PhysRevMaterials.8.084407.
[22] X. Liu, X. Shao, B. Yang, M. Zhao, Negative Poisson's ratio and high-mobility transport anisotropy in SiC_6 siligraphene, Nanoscale 10 (2018) 2108–2114, https://doi.org/10.1039/C7NR06932D.
[23] L. Yu, Y. Wang, X. Zheng, H. Wang, Z. Qin, G. Qin, Emerging negative Poisson's ratio driven by strong intralayer interaction response in rectangular transition metal chalcogenides, Appl. Surf. Sci. 610 (2023) 155478, https://doi.org/10.1016/j.apsusc.2022.155478.
[24] Z. Sun, Y. Su, A. Zhi, Z. Gao, X. Han, K. Wu, L. Bao, Y. Huang, Y. Shi, X. Bai, P. Cheng, L. Chen, K. Wu, X. Tian, C. Wu, B. Feng, Evidence for multiferroicity in single-layer CuCrSe2, Nat. Commun. 15 (2024) 4252, https://doi.org/10.1038/s41467-024-48636-z.
[25] P. Wang, Y. Zhao, R. Na, W. Dong, J. Duan, Y. Cheng, B. Xu, D. Kong, J. Liu, S. Du, C. Zhao, Y. Yang, L. Lv, Q. Hu, H. Ai, Y. Xiong, V.S. Stolyarov, S. Zheng, Y. Zhou, F. Deng, J. Zhou, Chemical Vapor Deposition Synthesis of Intrinsic High-Temperature Ferroelectric 2D $CuCrSe_2$, Adv. Mater. 36 (2024) 2400655, https://doi.org/10.1002/adma.202400655.
[26] T. Zhong, X. Li, M. Wu, J.-M. Liu, Room-temperature multiferroicity and diversified magnetoelectric couplings in 2D materials, Natl. Sci. Rev. 7 (2020) 373–380, https://doi.org/10.1093/nsr/nwz169.
[27] D. Srivastava, G.C. Tewari, M. Karppinen, R.M. Nieminen, First-principles study of layered antiferromagnetic $CuCrX_2$ (X = S, Se and Te), J. Phys. Condens. Matter 25 (2013) 105504, https://doi.org/10.1088/0953-8984/25/10/105504.
[28] J.L. Niedziela, D. Bansal, A.F. May, J. Ding, T. Lanigan-Atkins, G. Ehlers, D. L. Abernathy, A. Said, O. Delaire, Selective breakdown of phonon quasiparticles across superionic transition in CuCrSe2, Nat. Phys. 15 (2019) 73–78, https://doi.org/10.1038/s41567-018-0298-2.
[29] K.S. Rana, A. Singh, A. Bhui, K. Biswas, A. Soni, Anharmonic Phonon Vibrations of Ag and Cu for Poor Lattice Thermal Conductivity in Superionic $AgCrSe_2$ and $CuCrSe_2$, ACS Appl. Energy Mater. 7 (2024) 5621–5628, https://doi.org/10.1021/acsaem.4c01148.
[30] S. Bhattacharya, R. Basu, R. Bhatt, S. Pitale, A. Singh, D.K. Aswal, S.K. Gupta, M. Navaneethan, Y. Hayakawa, CuCrSe2: a high performance phonon glass and electron crystal thermoelectric material, J. Mater. Chem. A 1 (2013) 11289, https://doi.org/10.1039/c3ta11903c.
[31] G. Kresse, J. Furthmüller, Efficient iterative schemes for*ab initio*total-energy calculations using a plane-wave basis set, Phys. Rev. B 54 (1996) 11169–11186, https://doi.org/10.1103/physrevb.54.11169.
[32] G. Kresse, J. Furthmüller, Efficiency of ab-initio total energy calculations for metals and semiconductors using a plane-wave basis set, Comput. Mater. Sci. 6 (1996) 15–50, https://doi.org/10.1016/0927-0256(96)00008-0.
[33] P.E. Blöchl, Projector augmented-wave method, Phys. Rev. B 50 (1994) 17953–17979, https://doi.org/10.1103/physrevb.50.17953.
[34] J.P. Perdew, K. Burke, M. Ernzerhof, Generalized Gradient Approximation Made Simple, Phys. Rev. Lett. 77 (1996) 3865–3868, https://doi.org/10.1103/physrevlett.77.3865.
[35] A. Togo, L. Chaput, T. Tadano, I. Tanaka, Implementation strategies in phonopy and phono3py, J. Phys. Condens. Matter 35 (2023) 353001, https://doi.org/10.1088/1361-648X/acd831.
[36] A. Togo, First-principles Phonon Calculations with Phonopy and Phono3py, J. Phys. Soc. Jpn. 92 (2023) 012001, https://doi.org/10.7566/JPSJ.92.012001.
[37] R. Nelson, C. Ertural, J. George, V.L. Deringer, G. Hautier, R. Dronskowski, LOBSTER: Local orbital projections, atomic charges, and chemical-bonding analysis from PROJECTOR-AUGMENTED-WAVE-BASED density-functional theory, J. Comput. Chem. 41 (2020) 1931–1940, https://doi.org/10.1002/jcc.26353.
[38] V. Wang, N. Xu, J.-C. Liu, G. Tang, W.-T. Geng, VASPKIT: A user-friendly interface facilitating high-throughput computing and analysis using VASP code, Comput. Phys. Commun. 267 (2021) 108033, https://doi.org/10.1016/j.cpc.2021.108033.
[39] K. Momma, F. Izumi, *VESTA3*for three-dimensional visualization of crystal, volumetric and morphology data, J. Appl. Crystallogr. 44 (2011) 1272–1276, https://doi.org/10.1107/s0021889811038970.
[40] X. Shen, M.M. Koza, Y. Tung, N. Ouyang, C. Yang, C. Wang, Y. Chen, K. Willa, R. Heid, X. Zhou, F. Weber, Soft Phonon Mode Triggering Fast Ag Diffusion in Superionic Argyrodite Ag_8GeSe_6, Small 19 (2023) 2305048, https://doi.org/10.1002/smll.202305048.
[41] E. Ziambaras, E. Schröder, Theory for structure and bulk modulus determination, Phys. Rev. B 68 (2003) 064112, https://doi.org/10.1103/PhysRevB.68.064112.
[42] A. Marmier, Z.A.D. Lethbridge, R.I. Walton, C.W. Smith, S.C. Parker, K.E. Evans, ElAM: A computer program for the analysis and representation of anisotropic elastic properties, Comput. Phys. Commun. 181 (2010) 2102–2115, https://doi.org/10.1016/j.cpc.2010.08.033.